

Ergodic dynamics and thermalization in an isolated quantum system

C. Neill^{1,*} P. Roushan^{2,*} M. Fang^{1,*} Y. Chen^{2,*} M. Kolodrubetz³, Z. Chen¹, A. Megrant², R. Barends²,

B. Campbell¹, B. Chiaro¹, A. Dunsworth¹, E. Jeffrey², J. Kelly², J. Mutus², P. J. J. O’Malley¹, C. Quintana¹, D. Sank², A. Vainsencher¹, J. Wenner¹, T. C. White², A. Polkovnikov³, and J. M. Martinis^{1,2†}

¹Department of Physics, University of California, Santa Barbara, CA 93106-9530, USA

²Google Inc., Santa Barbara, CA 93117, USA and

³Department of Physics, Boston University, Boston, MA 02215, USA

I. QUBIT ARCHITECTURE

There are two fundamental requirements for implementing the quantum dynamics demonstrated in this work: a high level of individual control and long coherence times. In pursuit of these goals, we have designed three transmon qubits with tunable qubit-qubit coupling, tunable frequencies and individual microwave control [1]. Transmon qubits, the Xmon design in particular, have been shown to have long coherence times [2–4]. The qubits are arranged into a ring in order to explore the model outlined in the main text beyond the more technologically straight-forward two-qubit realization.

A circuit diagram and optical micrographs of our gmon qubits are shown in Fig. S1. The individual qubits are composed of a capacitor (red), a DC SQUID (blue), and two inductors in series to ground (green). The capacitor and SQUID form the basis of the standard Xmon qubit with the added inductors each allowing for tunable coupling to a neighboring qubit.

Tunable coupling is achieved through a mutual inductance to a loop containing a Josephson junction (cyan). This loop mediates the interaction between pairs of qubits. An excitation in either qubit generates a current in this loop which then excites the neighboring qubit. The strength of the qubit-qubit interaction g is modulated by applying a flux to the coupler loop; this flux sets the effective junction inductance. If the junction inductance is large, then a smaller current will flow through the coupler loop and the coupling will become weaker. For this device, the interaction strengths $g/2\pi$ were tunable from $+5$ MHz to -15 MHz; a value of -5 MHz was used for all of the experiments.

The energy decay times T_1 for all three qubits are shown in Fig. S2 versus qubit frequency. During the thermalization experiments, the qubits were operated near 5.7 GHz where the decay times of the three qubits were between 12 and 18 μ s. Each experimental sequence ran for at most 500 ns, excluding measurement. The time scales of the experiment were an order of magnitude below the energy decay times. The single-qubit dephasing times measured with Ramsey, however, ranged between 2 to 4 μ s, closer to the relevant time scales of the experiment. In the single qubit experiments shown in Fig 2 of

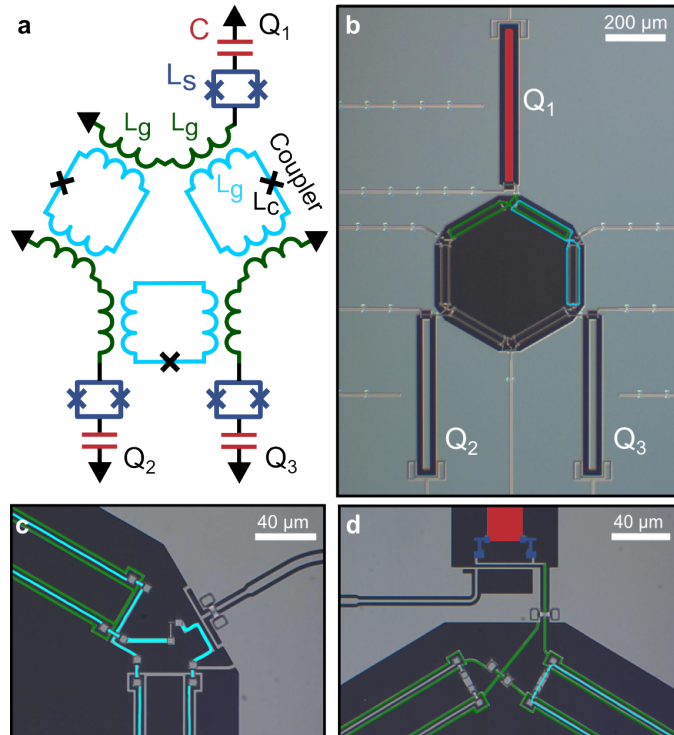


Figure S1. gmon architecture. We have designed a modified version of an Xmon qubit with tunable inter-qubit coupling. Panel **a** shows the circuit diagram for the device. Each qubit is represented as a capacitor ($C = 75$ fF) in series with a DC SQUID ($L_S = 8.1$ nH) and two inductors ($L_g = 0.35$ nH). Each inductor is flux coupled to an RF SQUID (‘coupler’) through a mutual inductance ($M = 0.2$ nH). Applying a flux to the RF SQUID loop modulates the effective junction inductance ($L_C = 0.9$ nH) and consequently the inter-qubit coupling strength. The effective SQUID inductances are the values at zero external flux. **b**, Optical micrograph of the device. Grey regions correspond to aluminum; black regions are where the aluminum has been etched away to expose the underlying sapphire substrate to define the qubits and wiring. **c,d**, Optical micrographs showing the coupler and qubit flux biases. The qubit and coupler inductors L_g can be seen highlighted in green and cyan, respectively. All crossover connections are made using dielectric-free airbridges [5].

the main text, decoherence is indistinguishable from entanglement with the other qubits. Measurements of the full three-qubit density matrix, however, allow us to sepa-

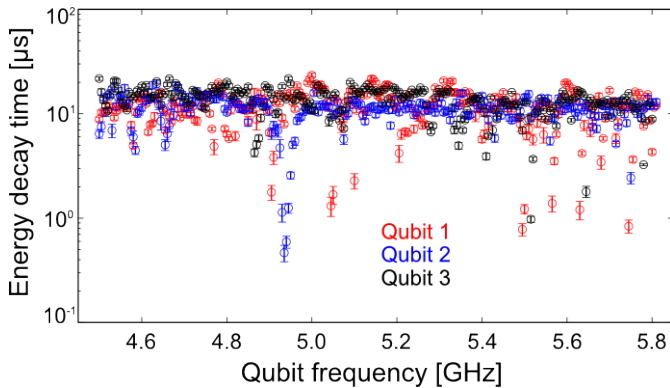


Figure S2. **Energy decay time T_1 .** The energy decay time of each qubit as a function of the qubit frequency. Each data point is measured by exciting the qubit, detuning it to the desired frequency, waiting a variable delay time, measuring the qubit excited state probability and fitting the decay curve to an exponential. The experimental results in this work were obtained near 5.7 GHz where the decay times ranged from 12 to 18 μ s.

rate decoherence from entanglement through multi-qubit correlation functions [6].

II. PULSE SEQUENCE

In Fig. S3 we show the pulse sequence and corresponding control waveforms used to implement the experiments in the main text. The pulse sequence can be broken up into three sections: state preparation, evolution and measurement. The initial states $|\theta_0, \phi_0\rangle$ were prepared in 40 ns using resonant microwave pulses, shown as a red oscillatory signal in the lower panel. The amplitude and length of the microwave pulse set the angle θ_0 ; the phase of the microwave pulse sets ϕ_0 . Each time step in the evolution then consists of two parts: a y -rotation and a symmetric three-qubit interaction. The y -rotation is achieved in 20 ns using a resonant microwave pulse shown in blue. The three-qubit interaction is performed by applying a square pulse to each coupling circuit, the duration of which sets κ . During the interaction, square pulses are used to maintain the qubits on resonance with one another as the coupler pulses cause the qubits to shift in frequency. We additionally calibrate for cross-talk between the six low-frequency control lines: three lines which tune the qubit frequencies and three which tune the coupling. The cross-talk matrix dV defined as

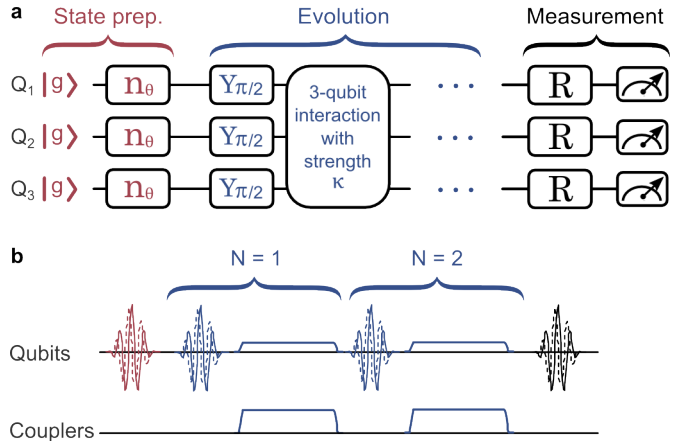


Figure S3. **Pulse sequence and control waveforms.** **a**, Gate sequence used to study ergodic dynamics and thermalization. First, each qubit is prepared in the ground state by waiting several energy decay times. Next, we rotate each qubit into the state $|\theta_0, \phi_0\rangle$ through a rotation around the axis $n = -\sin(\phi_0)\hat{x} + \cos(\phi_0)\hat{y}$ by angle θ_0 . This initial state is then evolved by N applications of a rotation around the y -axis by $\pi/2$ and a symmetric multi-qubit interaction. Following the evolution, the density matrix of either individual qubits or of the full system is determined using state tomography. State tomography consists of a rotation followed by a measurement along the z -axis. This is repeated for different rotation angles and axes to reconstruct the density matrix. **b**, The control waveforms used to implement the gate sequence are shown for $N = 2$. Oscillatory signals correspond to resonant microwave pulses used to rotate the single-qubit states. The amplitude and phase of the control waveform determine the rotation angle and axis respectively. Square pulses applied to the coupler and qubit SQUID loops are used to turn on the multi-qubit interaction and to maintain the qubits on resonance.

$V_{\text{actual}} = (1 + dV) V_{\text{ideal}}$ was measured to be

$$dV = \begin{pmatrix} \text{cp12} & \text{cp23} & \text{cp31} & \text{q1} & \text{q2} & \text{q3} \\ 0.00 & 0.09 & 0.07 & -0.08 & -0.05 & 0.15 \\ 0.03 & 0.00 & 0.05 & 0.14 & 0.06 & -0.07 \\ 0.09 & 0.11 & 0.00 & -0.35 & 0.15 & -0.04 \\ 0.04 & 0.00 & -0.05 & 0.00 & 0.05 & -0.04 \\ -0.02 & 0.02 & 0.02 & 0.01 & 0.00 & 0.03 \\ 0.02 & 0.02 & -0.02 & -0.01 & 0.04 & 0.00 \end{pmatrix}$$

After evolving the system forward N times, we reconstruct the density matrix of the qubits using state tomography. State tomography consists of single qubit rotations, shown in black, followed by measurements along the z -axis; this is then repeated for various rotation axes and angles. The rotations are chosen from a set of four rotations containing I , $X_{\pi/2}$, $Y_{\pi/2}$, and X_{π} . The measured z -projections are then used along with maximum likelihood estimates to construct a physical density matrix [7].

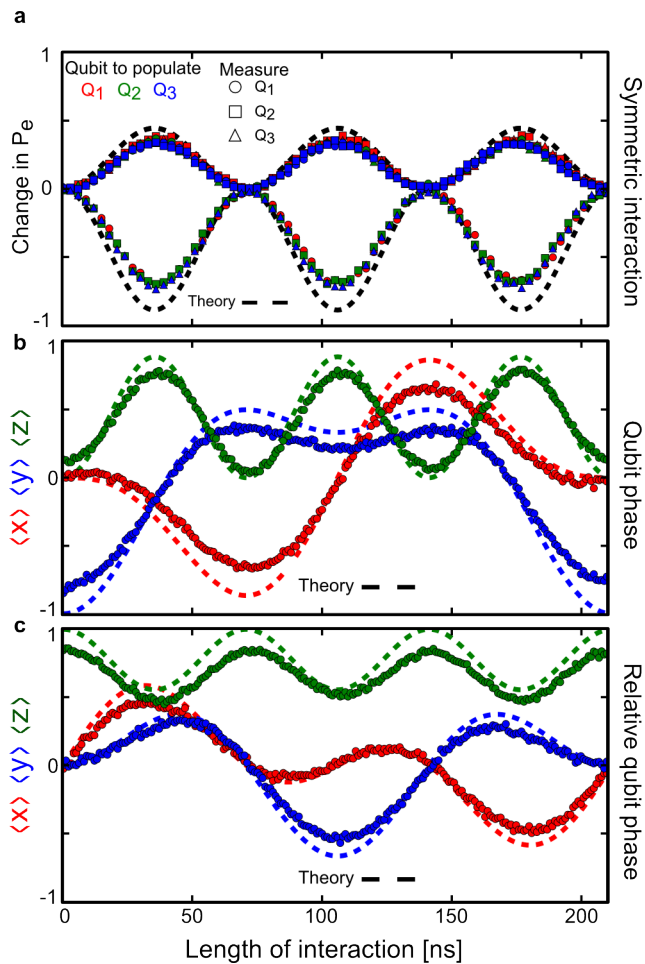


Figure S4. Characterizing the 3-qubit interaction. **a**, Here we demonstrate that the inter-qubit interaction energies are all of equal strength and that the qubits are on resonance during the interaction. This is done by exciting a single qubit, turning on the interaction for a variable length of time (horizontal axis) and then measuring all three qubit excited state probabilities P_e . We plot the change in P_e relative to having waited the corresponding length of time. We then repeat the experiment exciting different qubits, resulting in a total of 9 curves. The symmetry of the curves and the periodically going to zero indicate that the gate is properly calibrated. **b**, Here we demonstrate that we have corrected for changes in the single qubit phase that result from the interaction gate. We rotate one qubit to the equator of the Bloch sphere, turn on the interaction for a variable length of time, and then perform state tomography on the qubit which we rotated. The agreement with theory indicates that the phase is being properly corrected for. **c**, The relative control phases of the different microwave signals also needs to be corrected for. Here we rotate one qubit to the equator of the Bloch sphere, turn on the interaction for a variable length of time, and then perform state tomography on a neighboring qubit. The agreement of the curves with theory indicates that we have properly calibrated for this phase difference.

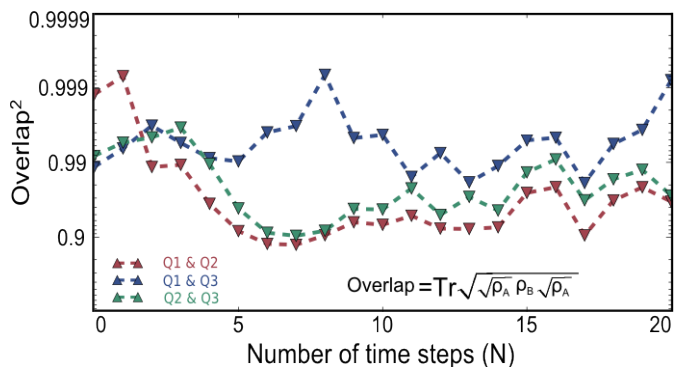


Figure S5. Symmetric evolution. We measure the single qubit density matrices as a function of the number of time steps N for $\kappa = 2.5$. At each time, we compute the overlap of the individual single qubit density matrices and plot the results.

III. SIMULTANEOUS THREE-QUBIT INTERACTION

The characterization procedure for the simultaneous three-qubit interaction is shown in Fig. S4. This procedure is broken up into three steps. First, we calibrate the six square pulse amplitudes (three qubits, three couplers) to ensure that the interaction strengths are all equal and that the qubits are on resonance. Second, these pulses can cause the qubits to detune from the microwave source; measuring this detuning allows us to correct for the resulting phase accumulation. Third, if there is a relative phase between the control signals on different qubits, this also needs to be corrected for.

The first experiment, shown in panel (a), demonstrates that the interaction energies are symmetric and that the qubits are on resonance. We begin by putting one of the qubits into its excited state, turning on the interaction for a variable length of time, and then measuring all three qubit excited state probabilities P_e . This experiment is then repeated exciting a different qubit each time; all 9 curves are plotted as a function of interaction length. In order to isolate the effects of interaction, we measure P_e as a function of time, without interactions, and subtract the results. If the qubits are detuned or the interaction strengths differ from one another, then the curves will not lie on top of each other. Additionally, both error sources will prevent the probabilities from returning to zero periodically. The data suggests that errors in the coupling and detuning are small over relevant time scales.

Measurements of P_e alone do not provide information about the phase of the qubit. In panel (b), we rotate one qubit to the equator of the Bloch sphere, turn on the interaction for a variable length of time, and then perform state tomography on the qubit which was rotated; we plot the expectation values of the single qubit Pauli operators. If the qubit is accumulating a phase during the

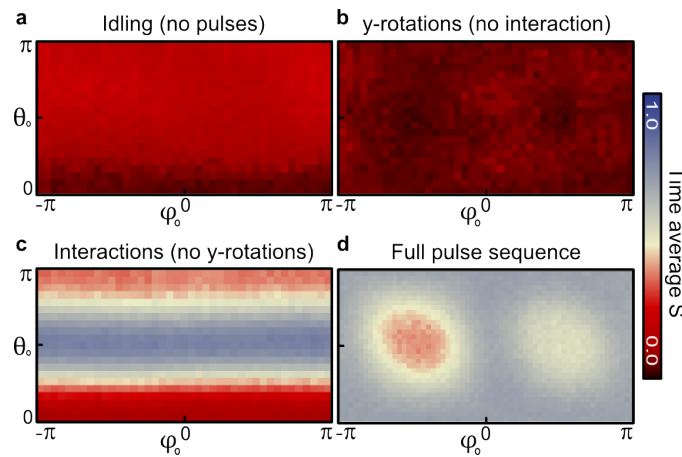


Figure S6. Dissecting the phase space dynamics. In all four panels we plot the time-average entanglement entropy of a single qubit versus initial state for $N = 20$ and $\kappa = 0.5$. To better understand the results, we consider four different pulse sequences: no pulses (just waiting), only y -rotations (no interactions), only interactions (no rotations), and both interactions and rotations. **a**, Average entanglement entropy after waiting a length of time equivalent to the full pulse sequence. **b**, Here, we apply only the y -rotations and replace the interactions with a wait of equivalent length. **c**, Now we perform the opposite experiment, applying only the interactions and wait instead of rotating. **d**, We now apply the full pulse sequence.

interaction as a result of detuning from the microwave source, then $\langle x \rangle$ and $\langle y \rangle$ will rotate into one another. We determine the rate of phase accumulation by measuring $\langle y \rangle$ for a 210 ns interaction length as a function of the phase accumulation rate correction and look for a minimum, as $\langle y \rangle$ is ideally minimum for this choice of interaction length. Correcting for this results in tomography which agrees well with an ideal operation; deviations result primarily from measurement visibility.

In panel (c), we rotate one qubit to the equator of the Bloch sphere, turn on the interaction for a variable length of time, and then perform state tomography on a neighboring qubit. If the relative phase of the microwave control signals on the individual qubits is non-zero, then the measured $\langle x \rangle$ and $\langle y \rangle$ values will rotate into one another. This may result from differences in electrical path lengths in the two control lines. We determine this phase by measuring $\langle y \rangle$ for a 105 ns interaction length as a function of the relative phase and look for a minimum. Correcting for this static phase difference results in tomography which agrees well with an ideal operation.

IV. QUBIT DYNAMICS

This three-qubit interaction along with local rotations are used to generate the dynamics that were explored in this experiment. As both the initial state and the evolu-

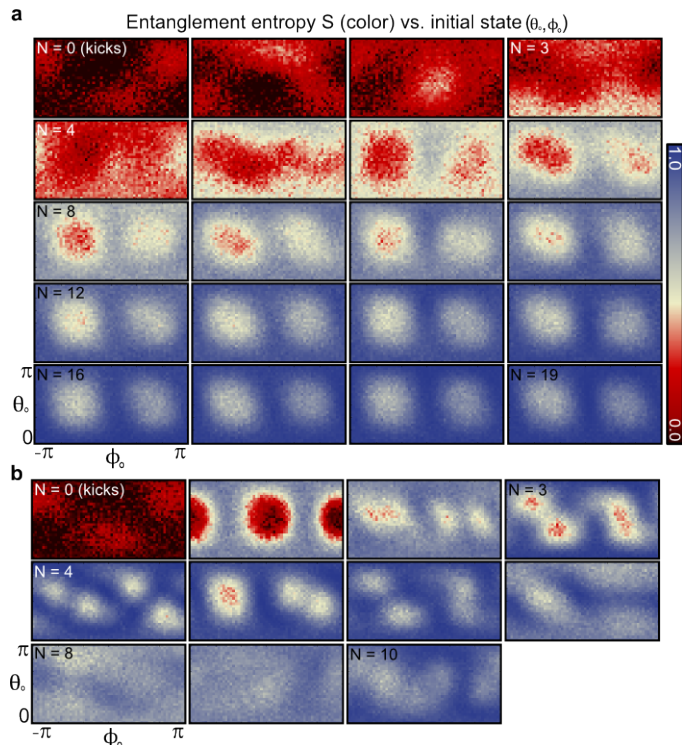


Figure S7. Snapshots of entanglement entropy. **a**, Entanglement entropy of a single qubit as a function of initial state for $N = 0$ to 19 at $\kappa = 0.5$. **b**, We repeat the experiment for $N = 0$ to 10 at $\kappa = 2.5$.

tion operators are symmetric under exchange of qubits, we expect to observe nominally identical behavior. In order to verify this, we measure the reduced density matrix of the individual qubits and compute their overlap. The results are shown in Fig. S5 for $\kappa = 2.5$ and an initial state along the z -axis. We find that the qubits remain symmetric over the length of the evolution.

The evolution of the qubits involves both a rotation and an interaction. In Fig. S6 we explore the effect of these pulses on the entanglement entropy of the individual qubits. In panel (a) we plot the time-average entropy versus initial state without either the rotation or interaction; instead, we simply wait for the corresponding length of time. For initial states near the ground state, the entropy is close to zero and increases slightly while approaching the excited state as a result of energy relaxation. In panel (b) we plot the same quantity, however, now we apply only the rotations without the interactions. Here, the entropy is uniform over initial states as the rotations average the results over many states. In panel (c), we apply only the interaction without the rotations. We see that near the ground or excited states the entropy stays near-minimum as the qubits do not entangle here. For initial states closer to the equator, we see an entanglement entropy near a half. Putting the interaction and the rotation together we recover the results shown in the

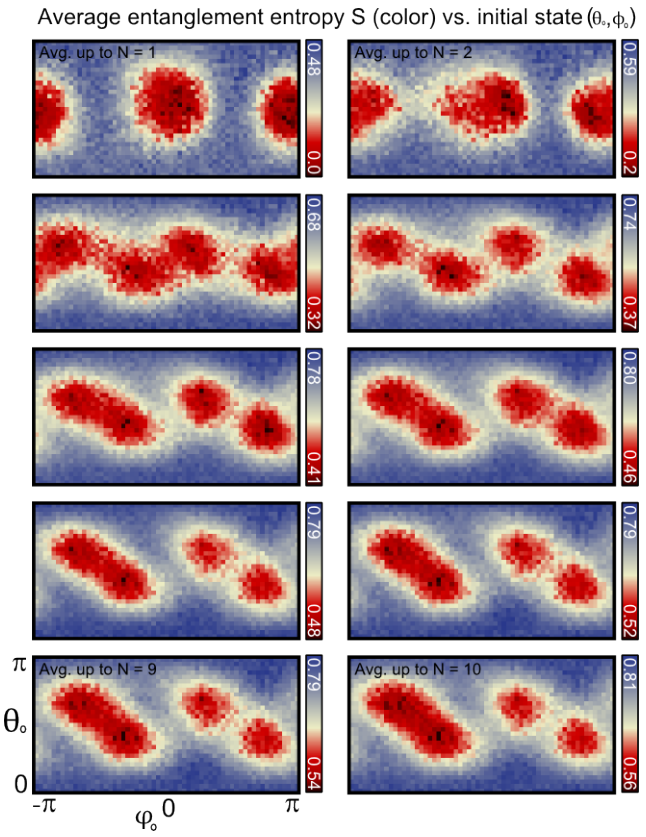


Figure S8. **Entanglement entropy, convergence with number of averages.** Entanglement entropy of a single qubit as a function of initial state at $\kappa = 2.5$. In the different panels, we increase the number of time steps over which we average the entropy. We find that the entanglement entropy qualitatively converges to the long time behavior after merely four time steps.

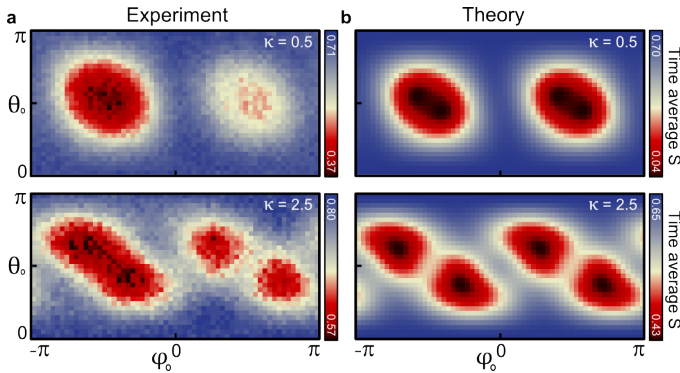


Figure S9. **Entanglement entropy, comparison with theory.** **a**, The time-average entanglement entropy of a single qubit versus initial state for $\kappa = 0.5$ (top) and $\kappa = 2.5$ (bottom) **b**, For comparison, we numerically compute the expected behavior and plot the results.

main text.

In Fig. 2 of the main text, we show the entanglement entropy at single instances in time for $N = 1, 3, 5$ and 7 for

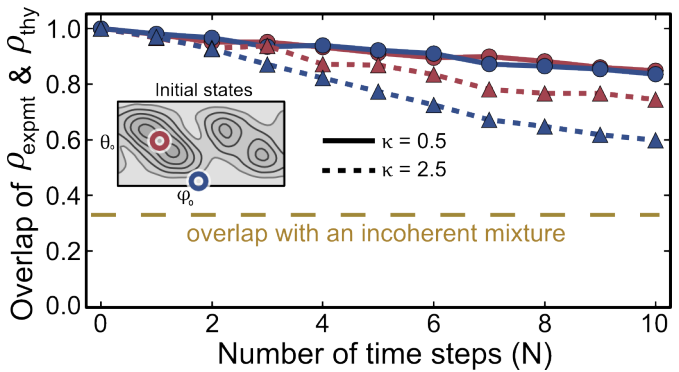


Figure S10. **Comparison with theory.** We measure the three-qubit density matrix for two initial states, one where subsystems thermalized (blue) and one where subsystems did not thermalize (red). We plot the overlap of the experimental density matrix ρ_{expt} and the theoretical density matrix ρ_{thy} calculated using the model presented in the main text.

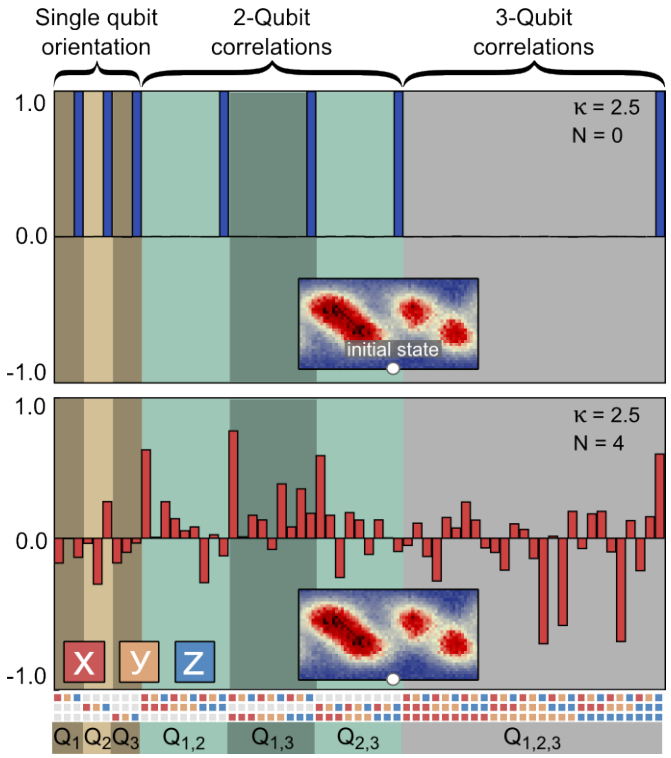


Figure S11. **Pauli representation.** We represent the three-qubit density matrix for an initial state shown inset and $\kappa = 2.5$. Each bar indicates the expectation value of one possible combination of Pauli operators on the three qubits, the corresponding operator is shown using colored squares. The increase in multi-qubit correlations in the lower panel is the result of two- and three-qubit entanglement.

both $\kappa = 0.5$ and $\kappa = 2.5$. In Fig. S7, we show the data for all time steps from $N = 1$ to 20 for $\kappa = 0.5$ (a) and from $N = 1$ to 10 for $\kappa = 2.5$ (b). In Fig. S8, we vary the number of time steps over which we average the entanglement entropy. We find that the regions of high and low

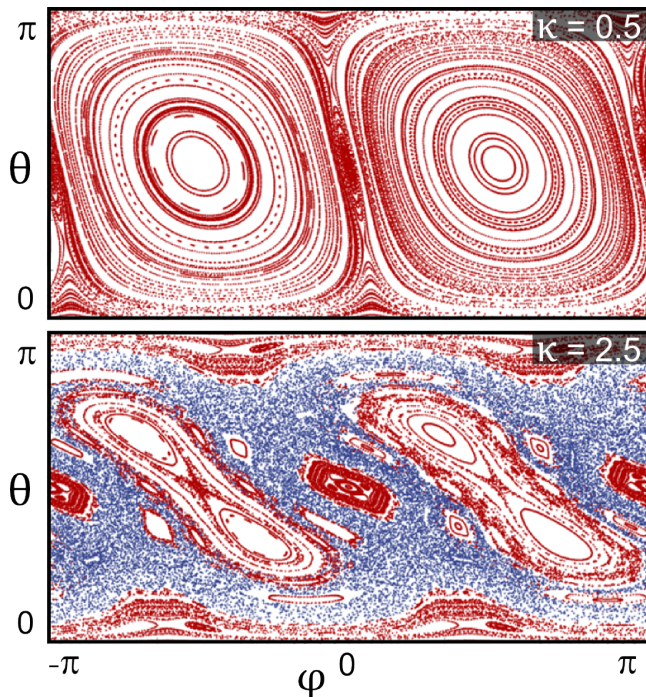


Figure S12. Classical lyapunov exponent. Numerical simulations of the classical phase space for $\kappa = 0.5$ (top) and $\kappa = 2.5$ (bottom). Red regions correspond to stable orbits and blue regions correspond to chaotic motion through the phase space. The two regions are distinguished using the maximum Lyapunov exponent.

entropy qualitatively approach the long time results after just four steps. In Fig. S9a, we show the entanglement entropy average over N , as shown in the main text. For comparison, we numerically compute the ideal behavior and show the results in Fig. S9b. The ideal behavior has a left/right symmetry that is not present in the experimental data. This is likely the result of control errors arising from imperfect calibrations and modifications to the dynamics resulting from dispersive shifts from higher states of the transmon qubit.

In Fig. S10 we consider the degree to which the model outlined in the main text describes the experimental results. Using the measured three-qubit density matrix ρ_{expt} , we compute the overlap of ρ_{expt} and the theoretically calculated density matrix ρ_{thy} . We plot the results as a function of time for two initial states, one where subsystems thermalized (blue) and one where subsystems did not thermalize (red), and for two values of interaction strength, $\kappa = 0.5$ and $\kappa = 2.5$.

In Fig. S11 we show the Pauli representation of the three-qubit density matrix for $\kappa = 2.5$. Initially, when $N = 0$, all of the single qubit states are along the Z axis and the remaining peaks reflect the corresponding classical correlations. After just a few kicks, however, the correlations are dominated by peaks that are not reflective of the single-qubit orientations.

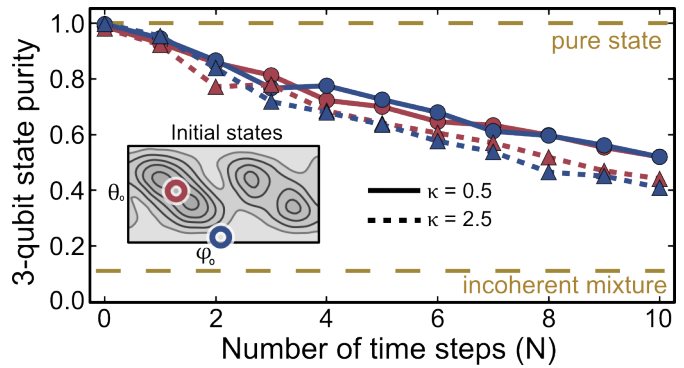


Figure S13. State purity as a measure of decoherence. We measure the three-qubit density matrix for two initial states, one where subsystems thermalized (blue) and one where subsystems did not thermalize (red). We plot the state purity, a measure of decoherence, as a function of the number of time-steps. We find that the decoherence is independent of initial state for all times and for both values of interaction strength $\kappa = 0.5$ and $\kappa = 2.5$. This suggests that the contrast between high and low entropy, entanglement and ergodicity found in the main text is the result of coherent quantum dynamics.

V. UNITARY DYNAMICS VS. DECOHERENCE

In the main text we show that single-qubit subsystems approach maximal entropy (i.e thermalize, Fig. 2) as a result of entanglement (Fig. 3). Additionally, we show that this occurs for initial states where time-averages are equal to state-space averages (i.e the dynamics are ergodic, Fig. 4). In contrast, we find that where the dynamics are less ergodic that subsystems do not thermalize or entangle. However, we have yet to determine if the contrast between high and low entropy, entanglement, and ergodicity results from unitary dynamics or environmental decoherence.

In Fig. S13 we show the state purity of the three-qubit density matrix ρ_{expt} as a function of time. We plot the purity for both an initial state where subsystems thermalized (blue) and did not thermalize (red). The state-purity, a measure of decoherence, is given by $\text{Tr } \rho_{\text{expt}}^2$ and is 1 for a pure state and $1/2^3$ for a three-qubit incoherent mixture. We find that the decoherence is independent of the initial state of the qubits. This result strongly suggests that the contrast in entropy, entanglement, and ergodicity is the result of coherent quantum dynamics.

VI. FINITE-SIZE SCALING

In statistical mechanics, fluctuations from equilibrium are expected to vanish with increasing system size. In our experiment, we average over these fluctuations in order to estimate the equilibrium value of entropy. In Fig. S14, we numerically show that these fluctuations in entropy over

time decrease as we consider larger systems. The points correspond to the standard deviation in entropy from $N = 10$ to 500 as a function of the number of spin-1/2 from 4 to 10. The solid line corresponds to the expected behavior from statistical mechanics where fluctuations decrease with the square root of system size. We find agreement between the fluctuations as computed from the quantum dynamics and the predictions from statistical mechanics.

A major achievement of statistical mechanics is the ability to predict the behavior of physical systems independent of their initial configuration. In our experiment, we show a clear difference in the entropy of initial quantum states whose classical limits are either chaotic or stable. If the system were thermal for all initial states, then we would not expect this state-dependent behavior. In Fig. S15, we consider larger values of interaction strength where the classical phase space is completely chaotic and compute the quantum evolution.

When the classical phase space is completely chaotic, we find the the entropy increases with system size independent of the initial state. This further supports the conclusion in the matin text that the observations correspond to a thermalization process.

* These authors contributed equally to this work.

† martinis@physics.ucsb.edu

- [1] Yu Chen, C. Neill, P. Roushan, N. Leung, M. Fang, R. Barends, J. Kelly, B. Campbell, Z. Chen, B. Chiaro, *et al.*, “Qubit architecture with high coherence and fast tunable coupling,” *Phys. Rev. Lett.* **113**, 220502 (2014).
- [2] R. Barends, J. Kelly, A. Megrant, D. Sank, E. Jeffrey, Yu Chen, Y. Yin, B. Chiaro, J. Mutus, C. Neill, *et al.*, “Coherent josephson qubit suitable for scalable quantum integrated circuits,” *Phys. Rev. Lett.* **111**, 080502 (2013).
- [3] R Barends, J Kelly, A Megrant, A Veitia, D Sank, E Jeffrey, TC White, J Mutus, AG Fowler, B Campbell, *et al.*, “Superconducting quantum circuits at the surface code threshold for fault tolerance,” *Nature* **508**, 500–503 (2014).
- [4] J. Koch, Y. Terri, J. Gambetta, A. Houck, D. Schuster, J. Majer, A. Blais, M. Devoret, S. Girvin, and R. Schoelkopf, “Charge-insensitive qubit design derived from the cooper pair box,” *Phys. Rev. A* **76**, 042319 (2007).
- [5] Z. Chen, A. Megrant, J. Kelly, R. Barends, J. Bochmann, Y. Chen, B. Chiaro, A. Dunsworth, E. Jeffrey, J. Mutus, and et. al., “Fabrication and characterization of aluminum airbridges for superconducting microwave circuits,” *App. Phys. Lett.* **104**, 052602 (2014).
- [6] J. Chow, “Quantum information processing with superconducting qubits,” PhD dissertation, Yale (2010).
- [7] M. Neeley, R. C Bialczak, M. Lenander, E. Lucero, M. Mariantoni, A. O’Connell, D. Sank, H. Wang, M. Weides, J. Wenner, *et al.*, “Generation of three-qubit entangled states using superconducting phase qubits,” *Nature* **467**, 570–573 (2010).

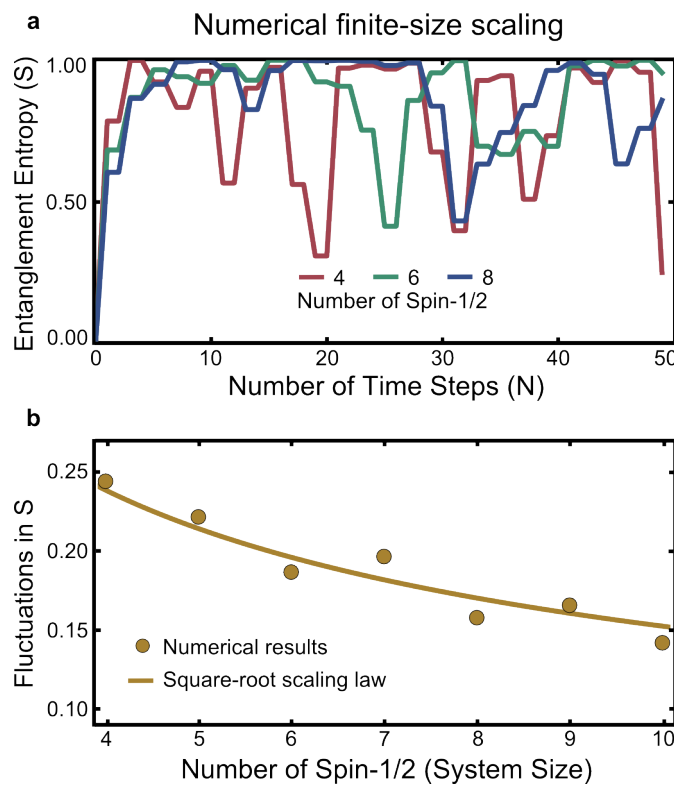


Figure S14. Decreasing fluctuations with system size. **a**, We numerically compute the entanglement entropy S versus the number of time steps N for increasing number of qubits. In all cases, the entropy approaches 1.0 after a few steps. However, there are significant fluctuations from this value over time due to the small size of the system. **b**, In the lower panel, we numerically compute the standard deviation in entropy from $N = 10$ to 500 as a function of the number of qubits and show that fluctuations in entropy decrease with increasing system size. For comparison, we overlay a curve with the square-root of system-size behavior typically found in statistical mechanics.

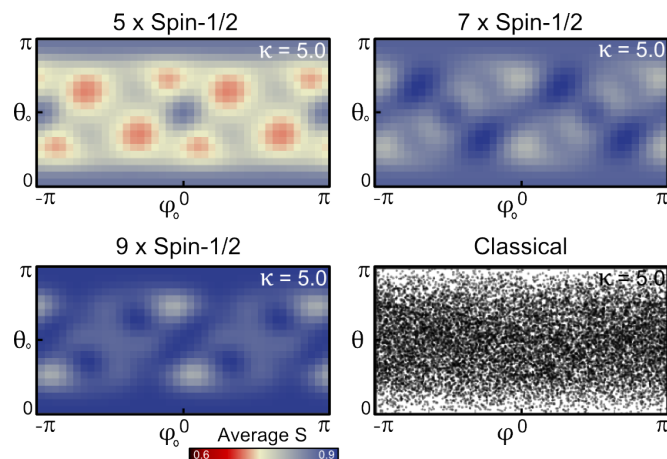


Figure S15. Thermalization for all initial states. We numerically compute the time-average entanglement entropy S as a function of initial state for an interaction energy $\kappa = 5.0$. The value of κ is chosen so that the classical phase space is no longer mixed but completely chaotic. In the first three panels we observe that the time-average entropy increases as a function of the number of spins, for all initial states. This suggests that at strong interaction all initial states thermalize in the limit of large systems. In the last panel (lower right), we show the classical phase space dynamics for comparison.